Spectroscopic observations, spin-orbit functions, and coupled-channel deperturbation analysis of data on the $A\ ^1\Sigma_u^+$ and $b\ ^3\Pi_u$ states of Rb_2

H. Salami and T. Bergeman
Department of Physics and Astronomy, SUNY, Stony Brook, New York 11794-3800, USA

B. Beser, J. Bai, E. H. Ahmed, S. Kotochigova, and A. M. Lyyra*
Department of Physics, Temple University, Philadelphia, Pennsylvania 19122, USA

J. Huennekens
Department of Physics, Lehigh University, Bethlehem, Pennsylvania 18015, USA

C. Lisdat
Physikalisch-Technische Bundesanstalt, Fachlabor 4.32, Bundesallee 100, 38116 Braunschweig, Germany

A. V. Stolyarov
Department of Chemistry, Moscow State University, GSP-2 Leninskie Gory 1/3, Moscow 119992, Russia

O. Dulieu
Laboratoire Aimé Cotton, CNRS, Université Paris-Sud, Bât. 505, 91405 Orsay Cedex, France

P. Crozet and A. J. Ross
Université de Lyon, Laboratoire de Spectrometrie Ionique et Moléculaire, UMR 5579 CNRS, Université Lyon 1, F-69622 Villeurbanne, France

(Received 7 February 2009; published 27 August 2009)

We present experimentally derived potential curves and spin-orbit interaction functions for the strongly perturbed $A\ ^1\Sigma_u^+$ and $b\ ^3\Pi_u$ states of the rubidium dimer. The results are based on laser-induced fluorescence and optical-optical double-resonance polarization spectroscopy measurements combined with earlier laser-induced fluorescence data. We used an analytic potential (Hannover form) incorporated in a discrete variable representation of the Hamiltonian matrix for numerical energy-level calculation. A previous vibrational assignment of the A levels is confirmed, and very probable vibrational assignment for the b levels is also obtained. Currently, the rms residual of our fit is 0.053 cm^{-1} as compared to the typical experimental uncertainties that are estimated to be 0.005 cm^{-1}. Fitted diagonal and off-diagonal spin-orbit functions are obtained and compared with *ab initio* calculations by all electrons and effective core pseudopotential methods. Analysis of the computational results yields an explanation for the ubiquitous single minima in these spin-orbit functions, which can be represented approximately by Morse-type functions.

DOI: 10.1103/PhysRevA.80.022515 PACS number(s): 33.20.Kf, 31.15.aj, 31.50.Df

I. INTRODUCTION

The lowest electronically excited states of alkali-metal dimers for long have been of interest as gateway or "window" states for the excitation of higher singlet or triplet levels [1]. Quite recently, various low-lying excited states of alkali-metal dimers have also been used as intermediaries in the production of ultracold molecules, as for RbCs [2], LiCs [3], KRb [4,5], Rb_2 [6], and Cs_2 [7–10]. Except for one recent case noted below, the lowest-excited states above the $^2S+^2S$ limit, namely, the $A\ ^1\Sigma_{(u)}^+$ and $b\ ^3\Pi_{(u)}$ states (where the ungerade designation applies only to homonuclear species), typically have not been used in such excitation schemes, partly because their energy-level structure is complicated by strong spin-orbit (SO) interactions. Recently, new methods [11–16] have been developed to analyze and model spectroscopic data on these highly perturbed states. As is evident from the discussion below, each effort to perform a "global analysis" of all available data on these two electronic states raises new questions about what Hamiltonian elements and functions are required and what data are required to determine the parameters so as to achieve a fit with residuals comparable to experimental uncertainties.

In regard to the effort to make ultracold molecules and Bose-Einstein condensates thereof, homonuclear species, such as Rb_2, do offer the interesting conceptual challenge of the effect of nonspherically symmetric particles in a condensate [17], and furthermore the cold atoms can be prepared with fewer lasers than required for dual-species systems. ^{87}Rb atoms were the first to be used for a dilute gas Bose-Einstein condensate [18], and they remain the most commonly used species for BEC studies. Photoexcitation of cold Rb atoms [19–21] primarily leads to long-range molecular states with energies near the $5\ ^2S+5\ ^2P$ limits. A character-

*Also at the Department of Physics, Lund Institute of Technology, Lund, Sweden.

ization of the lower parts of these potentials may be useful in modeling excitation transfer pathways from cold atoms to cold molecules. Spectral information on the lower levels of these states can only be obtained by excitation from thermal distributions of electronically ground-state molecules, as in a heatpipe oven or possibly a molecular beam.

As a route to cold ground-state molecules from a Feshbach resonance (FR), the A and b states of homonuclear species do not have the special advantage that they do for heteronuclear species, as discussed by Stwalley [22]. For homonuclear species, excitations from $a\ ^3\Sigma_u^+$ cannot go directly to either the $A\ ^1\Sigma_u^+$ or $b\ ^3\Pi_u$ *ungerade* states. There remains the possibility of using the $X\ ^1\Sigma_g^+$ component of a FR or cold atom collision to excite to the $A\ ^1\Sigma_u^+$ component of an upper-state level, as has been done recently with Cs_2 [9,10]. In the latter work, two two-photon steps were used to connect a FR level via $X(v=73,\ J=2)$ to $X(v=0,\ J=0)$ (efficient transfer is the next goal). Results of a detailed analysis of Cs_2 A-b state level structure [23] were used in [10] and such an analysis is clearly of interest for analogous experiments with Rb_2. The present study does not reach to very high levels of the A state that are directly excited from the most prominent Feshbach resonance but is a required first step.

There has been impressive progress in data acquisition and analysis for the heteronuclear A and b states from work on NaK [24–28] to more recent work on NaRb [14,29], NaCs [15], and RbCs [13]. For NaRb and NaCs, vibrational assignments of both states have been reliably determined, and the perturbative interactions have been modeled to an accuracy of 0.01 cm^{-1} or better. Higher-order spin-orbit effects were included in [15], and there was quite good agreement between empirically extracted and *ab initio* potentials. The heteronuclear alkali diatomics have attracted special interest because their ground-state permanent dipole moments offer interesting possibilities for studies of degenerate gases of ultracold particles with strong anisotropic interactions.

There has also been a succession of studies of the A and b states of the lighter homonuclear alkali dimer species Li_2 [30–33], Na_2 [16,34–37], and K_2 [11,12,38–41]. For Na_2 [16], data now extend almost continuously from the lowest vibrational levels to the atomic limit. An analysis of data on the A and b states of Cs_2 [23] noted above is in preparation. Regarding Rb_2, certain regular patterns in the level structure of the A and b states were observed [42], but a comprehensive analysis was not carried out.

This paper presents a detailed model of the energy-level structure of the A and b states of Rb_2. In all the above-cited studies of the A-b complex in alkali-metal dimers, the spin-orbit coupling functions are important elements because they produce singlet-triplet mixing and fine-structure splitting. Most (but not all) *ab initio* calculations of these particular molecular spin-orbit functions yield a function with a minimum significantly below the value at the asymptotic limit. This behavior has been approximated as a Morse function in empirical fits [16]. As there have been occasional dissenting suggestions, in this study we take pains to establish that this generic form holds both for empirical and *ab initio* spin-orbit functions, and we also suggest reasons why this form prevails.

This paper is organized as follows. In Sec. II, we describe experimental techniques used in Lyon and at Temple University to obtain high-resolution spectra. Section III describes the model used to fit the data. Section IV discusses fitted spin-orbit functions and also *ab initio* spin-orbit functions calculated from two different approaches, while Sec. V gives a short summary and conclusion.

II. EXPERIMENTAL DATA

Doppler limited absorption spectroscopy of the strong A-X system in heavier alkali-metal dimers yields rich spectra that are perturbed and incompletely resolved. The work performed here overcomes the latter problem either by recording sub-Doppler excitation spectra using optical-optical double-resonance (OODR) polarization spectroscopy or by recording high-resolution dispersed fluorescence. In both cases, upper-state term values are obtained by adding measured transition wave numbers to lower-state energies, which were determined accurately from the work of Seto *et al.* [43]. The experimental data in [43], from Laboratoire Aimé Cotton (LAC), had been obtained with the primary goal of accurately characterizing the ground $(X\ ^1\Sigma_g^+)$ state, and a by-product of this was the determination of several hundred upper-state $(A$-$b)$ term values. However, an accurate characterization of the levels of the A-b complex requires more extensive data than for the X state because there are two potentials and two spin-orbit functions rather than a single potential. To extend the data on the lowest vibrational levels of $A\ ^1\Sigma_u^+$, we performed additional observations of laser-induced fluorescence (LIF). In addition, our OODR polarization spectroscopy observations provide data on extended series of rotational levels, which were quite useful as noted below.

A. LIF data

The technique of dispersed laser-induced fluorescence is well suited to investigate strongly coupled A and b states of Rb_2. Levels of the $b\ ^3\Pi_u$ state below $v=0$ of the A state or with $\Omega^p \neq 0^+$ (i.e., levels that are *not* strongly mixed with the A state) are only weakly excited and do not fluoresce strongly enough for this technique to be effective. To obtain information on the lowest part of the A state potential, we excited molecules in low levels of the $X\ ^1\Sigma_g^+$ ground state to low vibrational levels of the $A\ ^1\Sigma_u^+$ state and used a Fourier transform interferometer for detection. A linear heatpipe was loaded with a ~ 1 g sample of Rb metal plus argon ($P=13$ Torr) as a buffer gas. The central zone (15 cm long) was maintained at 530 K. Fluorescence was excited with emission from a CR 899 (Coherent Inc.) Ti:sapphire laser equipped with long-range optics, at wavelengths 885–970 nm, concentrating particularly on the 0–6 and 1–6 A-X bands around 10 360 and 10 460 cm^{-1}. The laser could only be tuned manually (by adjustment of the cavity etalons) to select cavity modes, so the output wavelength was not necessarily in perfect resonance with a maximum of a molecular transition. Because of this, we estimate the wave-number uncertainty to be ± 0.005 cm^{-1} in the spectra, and this was

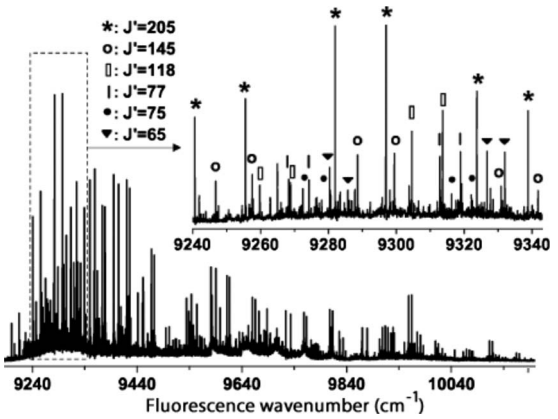

FIG. 1. FT laser-induced fluorescence spectrum from Lyon showing six $A \rightarrow X$ vibrational progressions excited by σ_{laser} = 11 150.55 cm^{-1}. In this figure, the $J'=118$ and 75 series are from $^{85}Rb^{87}Rb$, while the others are from $^{85}Rb_2$.

verified by the residuals obtained in the fitting procedure. Output power from the laser varied from 100 to 400 mW, according to etalon adjustments, but was in most cases close to 150 mW.

Backward fluorescence was recorded at an instrumental resolution ~0.05 cm^{-1} on a Fourier transform interferometer (Bomem DA3). Both Si-avalanche ($\lambda < 950$ nm) and InGaAs ($900 < \lambda < 1600$ nm) photodiode detectors were used. With the InGaAs detector, $\lambda > 950$, 1000, or 1100 nm filters reduced laser scatter from the heatpipe windows. The Si-avalanche detector records fluorescence to low vibrational levels of the ground state, where spectra were usually less complicated, while the InGaAs detector was invaluable since fluorescence is often strongest (and shows rotational relaxation) in transitions to high v' levels in the ground state. Spectra were recorded over a wide range (typically 2000 cm^{-1}) to measure sufficient rovibrational intervals to discriminate properly between isotopomers.

An example of an LIF+FTS spectrum of Rb_2 is given in Fig. 1. About 60 such spectra were recorded in Lyon. Typically, each contained fluorescence series from about 5 A-b levels. Some series included data with $\Delta J = \pm 2, \pm 4 \ldots \pm 14$, through rotational relaxation. From the parameters for the ground state [43], we have calculated the term values of the A state by adding the fluorescence transition energy to the energy of the excited rovibronic level of the ground state. The X state $\Delta G_{v,J}$ values are predicted to within 0.001 cm^{-1} from the parameters of [43], which imposes no limitation on the fivefold larger uncertainties we claim for the excited-state term values. About 450 new term values for the $^{85}Rb_2$ and $^{85}Rb^{87}Rb$ dimers have been added to previous data from LAC.

B. OODR polarization spectroscopy

The OODR polarization spectroscopy was performed at Temple University to explore more energy levels in the A-b complex and therefore to improve the quality of the overall fit to the A-b term value data. The two-color OODR polarization spectroscopy technique used here has been described in earlier papers [39], but in this work, weaker rotational satellites were recorded in addition to the R,P doublets expected from a single polarized ground state. Briefly, a V-type optical-optical double-resonance excitation scheme with independent pump and probe lasers was employed. A single mode cw CR 699–29 Autoscan DCM dye laser (power attenuated to ~30 mW) was the pump laser. The probe laser was a single mode cw CR 899–29 Autoscan Ti:sapphire laser (power attenuated to ~4 mW) with midwavelength optics. The stronger DCM dye laser (calibrated using an iodine atlas [44,45]) was set at a fixed frequency resonant with a few rovibronic transitions in the $B\ ^1\Pi_u$-$X\ ^1\Sigma_g^+$ system known from the high-resolution studies [46], thus, labeling a selection of rotational levels in the ground state. The Ti:sapphire probe beam calibrated using optogalvanic spectroscopy of uranium [47] was tuned across the $A\ ^1\Sigma_u^+ \leftarrow X\ ^1\Sigma_g^+$ band system, in the spectral range of 11 380–12 572 cm^{-1}.

The Rb_2 molecules were prepared in a heatpipe oven heated to 480 K with 1 Torr argon as a buffer gas. The stronger pump beam was circularly polarized by using a Babinet Soleil compensator (Karl Lambrecht). The linearly polarized probe beam and circularly polarized pump beam counterpropagated and crossed at the center of the heatpipe at a small angle. Crossed polarizers were placed in the path of the probe beam at either side of the heatpipe. When the probe and pump beams share a common (lower) level, the probe beam is affected by the optical anisotropy generated by the pump beam. Its polarization is modified and a small fraction of the beam passes through the second polarizer. A photomultiplier tube (Hamamatsu R928) detects the transmitted probe beam. Phase sensitive detection is performed with an SRS 850 lock-in amplifier set to the difference frequency of the pump and probe-laser beam modulation frequencies. The detection sensitivity was varied in order to enhance the signal from weak lines and thereby extract maximum information from the spectra. The information about the excitation spectrum is contained in the transmitted intensity of the probe light.

In the experiment presented in this work, molecules were pumped primarily by two strong $B \leftarrow X$ transitions which overlapped within their Doppler widths: the $B\ ^1\Pi_u(v'=2, J'=70) \leftarrow X\ ^1\Sigma_g^+(v''=0, J''=71)$ transition at 14 736.181 cm^{-1}, and the $B\ ^1\Pi_u(v'=2, J'=85) \leftarrow X\ ^1\Sigma_g^+(v'=0, J'=84)$ transition at 14 736.163 cm^{-1}, as obtained from the Dunham coefficients [43,46]. The measured laser wave number was 14 736.184 cm^{-1}.

The spectra (Fig. 2) were far more complicated than expected from these two strong pump transitions alone or with additional contributions from other possible (weaker) pump transitions. The additional lines were unexplained until we realized that the anisotropic M_J distribution survives collisional energy transfer [48], and all affected levels also serve as initial probe-laser excitation levels. Furthermore, since more highly excited states have not yet been mapped, there is no simple way to discriminate probe transitions that start from the pump upper level, so such transitions also appear in the spectra. Collisional transfer is not commonly observed in polarization spectroscopy, but many additional collision-induced probe transitions were recorded here because of the high signal-to-noise ratio and the high amplification applied to the transmitted signal.

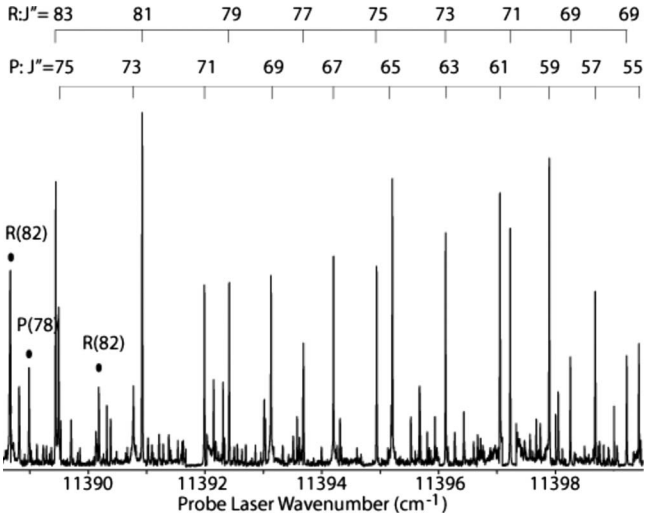

FIG. 2. A part of the OODR polarization spectroscopy of Rb_2 observed with circular polarization of the pump light. Two progressions figure in this plot. Most of the lines recorded here are associated with the $^{85}Rb_2$ $B\,^1\Pi(v'=2,J'=70)\leftarrow X\,^1\Sigma_g^+(v'=0,J'=71)$ pump transition. Ground-state J'' quantum numbers for R and P branches are indicated at the top. Probe transitions induced by the other pump excitation (at the same excitation frequency), $B\,^1\Pi(v'=2,J'=85)\leftarrow X\,^1\Sigma_g^+(v'=0,J'=84)$, are labeled $R(84)$, $P(76)$, and $R(82)$ toward the far left. [NB amplification was reduced for the strongest $P(71)$ and $R(71)$ lines; intensities are not scaled.]

C. Data summary

The range of the data used in this work is shown in Fig. 3. The assigned lines and fitted term values are given in the EPAPS data supplement [49]. In summary, there were 1413, 324, and 11 $^{85}Rb_2$, $^{85}Rb^{87}Rb$, and $^{87}Rb_2$ term values, respectively, in the data set. However, when internal duplications are considered, these numbers decrease to 829, 309, and 11. The data from Temple University consisted of $^{85}Rb_2$ P-R pairs, for example. 415, 338, and 454 distinct term values were obtained from LAC, Lyon, and Temple University, respectively, including 73 term values obtained from at least two laboratories. Clearly, it is advantageous to have data from different sources. Instances of duplicate observations from different experiments allowed self-consistent calibration procedures to be used.

III. ANALYSIS OF THE DATA

A. DVR Hamiltonian

The $A\,^1\Sigma_u^+$-$b\,^3\Pi_u(0_u^+)$ electronic states in the lighter alkali-metal dimers were first analyzed using traditional band-by-band methods [36], yielding $G(v)$, $B(v)$, and coupling parameters for many vibrational levels. This approach was extended [35] to include several nearby levels that are coupled together over a range of rotational quantum numbers. For the A and b states of K_2, this extended manifold approach was shown to be inadequate [11], and the merits of a multichannel approach were demonstrated, as also shown in [12]. Especially, when the coupling elements are larger than the vibrational energy intervals, significant coupling occurs between many levels, extending even to the continua. Therefore, a model based on a set of vibrational levels becomes cumbersome because it requires many $G(v)$, $B(v)$, and centrifugal distortion parameters, as well as coupling parameters and second-order perturbation sums.

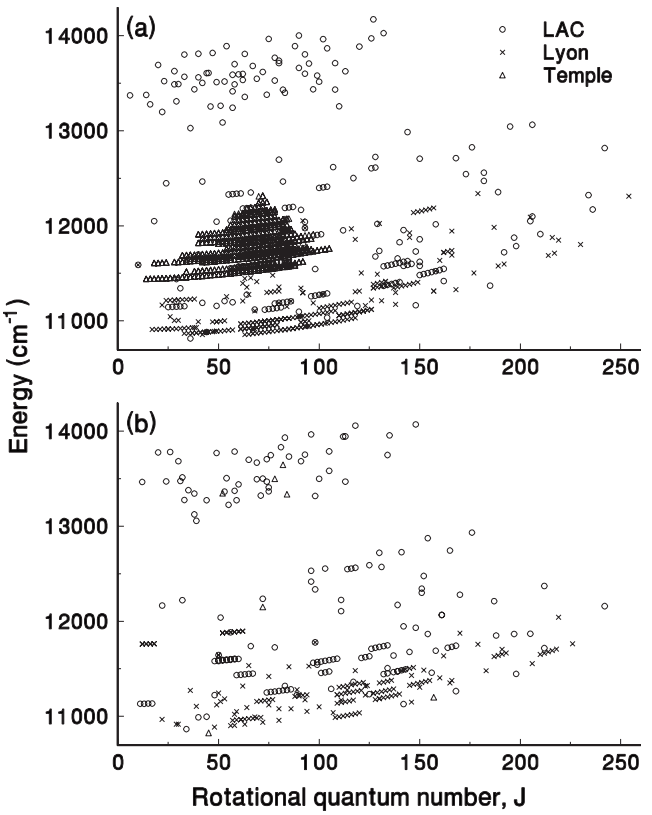

FIG. 3. Data set of the Rb_2 $A\,^1\Sigma_u^+$-$b\,^3\Pi_u$ state used for the deperturbation analysis. (a) $^{85}Rb_2$; (b) $^{85}Rb^{87}Rb$. Energies in this plot are relative to the minimum of the $X\,^1\Sigma_g^+$ ground state.

By contrast, numerical methods that generate the entire manifold of eigenstates for coupled Born-Oppenheimer potentials allow a simpler representation. Such methods were introduced some time ago in [50–52] and were first applied to diatomic molecular spectra in [53]. The terms "Fourier grid Hamiltonian" (FGH) and "discrete variable representation" (DVR) refer to similar techniques, but FGH uses a plane-wave basis and our particular DVR form uses particle-in-a-box basis functions. DVR methods have now been applied to a number of systems [11–13,16]. Alternative methods for computing the second derivative of the wave function for the kinetic-energy term in a multichannel approach have also been developed [14,15] and have yielded excellent results for the strongly coupled A and b states of NaRb and NaCs, respectively.

In the DVR approach, all mesh points rather than just 3 or 5 as in usual numerical differentiation procedures are used to obtain d^2/dR^2. The kinetic energy is obtained accurately with fewer total mesh points than required in other methods. The kinetic energy requires a full matrix over the mesh points for each channel, while the potential-energy elements and also spin-orbit coupling functions are diagonal over the mesh points. To reduce the required number of mesh points, the R

coordinate is scaled as discussed below and in [54].

The Hamiltonian that applies here consists of terms for kinetic energy H_K, potential energy H_V, rotation H_{rot}, and spin-orbit coupling H_{SO},

$$H = H_K + H_V + H_{rot} + H_{SO}. \tag{1}$$

Here $H_K = -(\hbar^2/2\mu)\ d^2/dR^2$, where R is the distance between two nuclei and μ is the reduced mass. The second derivative is evaluated with DVR [52], using a scaling function $y(R) = -R_0/(R+R_s)$, with inverse function $U(y) = -(R_s + R_0/y)$. As discussed in [54], after the transformation $\Psi(R) = \phi(y)/\sqrt{U'(y)}$, the kinetic-energy term operating on $\phi(y)$ becomes

$$H_K = -\frac{\hbar^2}{2\mu}\left\{\frac{1}{U'(y)}\frac{d^2}{dy^2}\frac{1}{U'(y)} + \frac{1}{2}\frac{U^{(3)}(y)}{[U'(y)]^3} - \frac{3}{4}\frac{[U^2(y)]^2}{[U'(y)]^4}\right\}. \tag{2}$$

It so happens that for the form of $U(y)$ chosen here, the last two terms within the bracket in Eq. (2) sum to zero. In this work, the values $R_0 = 1.0$ and $R_s = 2.16$ Å $(4a_0)$ were used.

In the y coordinate, the N DVR mesh points [52] are $y_i = y_{min} + i\Delta_y$; $\Delta_y = (y_{max} - y_{min})/(N+1)$. (The particle-in-box wave functions are identically zero at y_{min} and y_{max}.) We have found that the simpler expressions in [52] represent the second derivative with no loss of accuracy,

$$T_{ii'} = \frac{\hbar^2}{2\mu\Delta_y^2}(-1)^{i-i'} \times \begin{cases} \pi^2/3, & i = i' \\ \dfrac{2}{(i-i')^2}, & i \neq i'. \end{cases} \tag{3}$$

This form of the kinetic energy agrees with the expression obtained for Sinc collocation points in [55].

The matrix elements of $H_1 = H_V + H_{rot} + H_{SO}$ used in this work are

$$\begin{aligned}
\langle {}^1\Sigma^+|H_1|{}^1\Sigma^+\rangle &= V({}^1\Sigma^+) + (x+2)B, \\
\langle {}^3\Pi_\Omega|H_1|{}^3\Pi_\Omega\rangle &= V({}^3\Pi_0) + \Omega\Delta_d + (x+2\epsilon)B, \\
\langle {}^1\Sigma^+|H_1|{}^3\Pi_{0^+}\rangle &= -\Delta_{od}, \\
\langle {}^3\Pi_0|H_1|{}^3\Pi_1\rangle &= -\sqrt{2x}B, \\
\langle {}^3\Pi_1|H_1|{}^3\Pi_2\rangle &= -\sqrt{2(x-2)}B,
\end{aligned} \tag{4}$$

where $x = J(J+1)$, $\epsilon = 1$ for $\Omega = 0$ and 1, and -1 for $\Omega = 2$, and $H_1^\dagger = H_1$. In the above, $V({}^1\Sigma_u^+)$, $V({}^3\Pi_u)$, Δ_d, Δ_{od}, and $B = \hbar^2/(2\mu R^2)$ are functions of R. Δ_d and Δ_{od} are diagonal and off-diagonal spin-orbit functions, respectively.

Note that the above matrix elements agree with standard usage as in [56] except for two modifications. First, on the right-hand side of the second line of Eq. (4), the first two terms are $V({}^3\Pi_0) + \Omega\Delta_d$ rather than $V({}^3\Pi_1) + (\Omega-1)\Delta_d$ because the experimental data are primarily 0_u^+ character. The introduction of $\Omega = 2$ components into the Hamiltonian as given above is an approximation that neglects appreciable second-order spin-orbit shifts due to coupling to with $B\ {}^1\Pi_u$ and (2) ${}^3\Sigma_u^+$. Such shifts act on $V({}^3\Pi_{1u})$ but not $V({}^3\Pi_{2u})$ and thus destroy the equality in the fine-structure intervals indicated in Eq. (4). Since no data points were assigned as primarily $b\ {}^3\Pi_{2u}$ and since Coriolis coupling effects between $\Omega = 1$ and 2 levels are small here, this approximation was deemed acceptable. Second, the rotational terms in Eq. (4), as in [12,16,57], are obtained from a Hund's case e to case a transformation at the atomic limit, in anticipation of an extension of the present study to the dissociation limit so as to connect with the data in [20]. There are slight differences with respect to the forms given in [56] below Eq. (3.2.15), where $B(R)(\mathbf{L}^2 - \mathbf{L}_z^2)$ (z refers to the molecular axis) is included in the electronic energy and, hence, neglected in expressions for rotational energy, following traditional usage. Reference [57] assumes that for all R, $\mathbf{L}^2 = 2$ for molecular states tending to $S+P$ atoms. A more careful treatment might be to use *ab initio* estimates for the R dependence of this quantity, but actually the different convention amounts simply to a small shift of the T_e values.

Our DVR Hamiltonian matrix has a dimension equal to the number of R mesh points N times the number of channels j. Here, two-channel calculations include only ${}^1\Sigma_u^+$ and ${}^3\Pi_{0u+}$. For three-channel calculations, ${}^3\Pi_{1u}$ levels are added and then for four channels ${}^3\Pi_{2u}$ is also included. The $N \times N$ diagonal blocks map the kinetic and potential-energy operators for each of the coupled states, while the off-diagonal blocks (which themselves are diagonal) map the coupling operators. Note that for each J value, a separate diagonalization of the DVR matrix is required.

We have used the analytic expression adopted by the Hannover group [11,58] to represent the A and b potentials,

$$V_{SR}(R) = T_e + \sum_{k=2}^{K} a_k \left(\frac{R - R_e}{R + bR_e}\right)^k. \tag{5}$$

Having omitted a term in a_1 in Eq. (5), we can obtain

$$\frac{\partial^2 V}{\partial R^2}(R = R_e) = \frac{2a_2}{R_e^2(1+b)^2} \Rightarrow \omega_e = \frac{1}{10\pi(1+b)R_e}\left(\frac{ha_2}{2\mu c}\right)^{1/2}, \tag{6}$$

where μ, h, c, and R_e are in SI units, and a_k and ω_e are in cm^{-1}.

For the asymptotic regions, $R \leq R_L, R \geq R_R$, the potential in each case is given by

$$V_m(R) = c_m + \frac{d_m}{R^{\alpha_m}}; \quad m = A, b, \tag{7}$$

where c_m and d_m are chosen to make the potential and first derivative continuous at R_L or R_R, and α_m is chosen to preserve the general shape of the potential curves on either side of R_L or R_R. Because the data do not sample the potentials at R values near or beyond the Le Roy radius [59], the appropriate value of α_R is not equal to the asymptotic value of 3. Values of R_L and R_R are chosen so that $V_{A,b}(R_{L,R})$ are close to or above the turning points of the highest levels included in the fit; but for the $A\ {}^1\Sigma_u^+$ state, R_R was beyond the range of the data and the asymptotic form was not used.

Diagonal and off-diagonal spin-orbit functions for the A and b states of many alkali-metal dimers [12,14–16] and also for other states below the lowest ${}^2S + {}^2P$ threshold in NaK [28,60] and RbCs [61] have exhibited a significant minimum

at an R value somewhat greater than R_e. We discuss this feature further in Sec. IV. At this point, we state that for an approximate representation of this behavior, the diagonal and off-diagonal spin-orbit functions $\Delta_d(R)$ and $\Delta_{od}(R)$ have been modeled with the Morse form. With $i=d,od$,

$$\Delta_i(R) = p_i(2) + [p_i(1) - p_i(2)][1 - e^{p_i(4)[p_i(3)-R]}]^2. \quad (8)$$

The asymptotic spin-orbit splitting [$p_i(1)$ in this expression] can be obtained from the atomic fine-structure interval. The asymptotic values are known to be $\Delta/3$ for Δ_d and $\sqrt{2}\Delta/3$ for Δ_{od}, where Δ is the atomic fine-structure interval, which is 237.598 cm^{-1} for the Rb 5 ^2P state [62].

B. Fitting process and calculated term values

The process of fitting A and b state data discussed here began with 424 term values from LAC (given in the EPAPS supplementary data files from Ref. [43]). Also at LAC, a tentative vibrational numbering for the A state was obtained by shifting an *ab initio* potential by three vibrational quanta to obtain agreement between calculated Franck-Condon factors and observed fluorescence intensities. The rms residuals were approximately 3 cm^{-1} from this preliminary analysis. Acquisition of the additional data described in Sec. II has confirmed this vibrational numbering for the A state and led to more accurate estimates of the potentials and spin-orbit coupling functions.

Initial estimates for the potentials and spin-orbit functions came from the work in LAC, using *ab initio* calculations from [63,64]. In the early stages of our work, the model Hamiltonian included only $\Omega=0_u^+$ components from the $A\ ^1\Sigma_u^+$ and $b\ ^3\Pi_u$ states because there were very few term values that could be associated with $\Omega=1$ states. Later, the matrix was expanded to include $\Omega=1$ and 2 components, as discussed below. The range of R values was typically from 2.55 to 8.70 Å, and the energy limit was 14 200 cm^{-1}. In view of the scaling of the R coordinate [54], 340 mesh points sufficed for most of the calculations. For energies up to 13 500 cm^{-1}, calculations with this mesh agreed with calculations with 900 mesh points to within 1×10^{-4} cm^{-1}. For higher term values, the deviations between results from the smaller and larger mesh increased and were approximately 0.02 cm^{-1} at 14 200 cm^{-1}. Nevertheless, to expedite fitting, 340 mesh points were used except in the final stages, when a four-channel Hamiltonian with 500 mesh points in each channel was used.

In the beginning, the procedure consisted of fitting the lowest term energy values and varying just a few parameters to adjust the bottom of the potential wells. Progressively, more upper-state vibrational levels were added and, therefore, more parameters were fitted.

A key point in this analysis was the characterization of the $v=0$ level of the A state, much enhanced by the LIF data from Lyon. Eventually, the vibrational numbering of the $b\ ^3\Pi_{0u+}$ manifold was also established with a high degree of certainty. An rms residual of 0.053 cm^{-1} was obtained with the value of $T_e(b\ ^3\Pi_{0u+})=9600.50$ cm^{-1} given in Table I, which identifies the $J=0$ $b\ ^3\Pi_{0u+}$ level just below $A(v=0,J=0)$ as $v=20$. In contrast, when the vibrational numbering of the b manifold is decreased by one, the rms residual is 0.184 cm^{-1}, and when it is increased by one, the rms residual is 0.145 cm^{-1}. Although the strongly perturbed levels in this system do not exhibit unambiguously clear shifts with

TABLE I. Fitted parameters for the Rb_2 A and b potentials and for spin-orbit functions issued from four-channel calculation. T_e, ω_e (for $^{85}Rb_2$), the a_k, and $p_i(j), j=1,2$ are in cm^{-1}, R_e, and $p_i(3)$ are in Å, $p_i(4)$ are in $Å^{-1}$, and b is dimensionless. For the asymptotic regions, $m=L,R$, R_m are in Å, c_m are in cm^{-1}, α_m are dimensionless, and d_m are in $cm^{-1}\times Å_m^{\alpha}$. Numbers in square brackets denote the power of 10. Numbers in parentheses denote three times the standard deviation of the fitted parameter as quoted by the fitting program. The first line gives the approximate range of R values sampled by the data (in Å). c_R, etc., are omitted for the A state because the long-range form was not needed.

	$A\ ^1\Sigma_u^+$ state	$b\ ^3\Pi_{0u^+}$ state
R range	3.60–7.51	3.03–6.55
b	0.6	0.3
R_e	4.87368(21)	4.13157(120)
T_e	10749.742(39)	9600.83(900)
ω_e	44.58(12)	60.10(18)
a_2	0.76094557 [5]	0.65607823 [5]
a_3	−0.85201119[5]	−0.35800523[6]
a_4	−0.93357657[5]	0.33033356 [7]
a_5	0.15873909 [6]	−0.38950791[7]
a_6	−0.12640111[7]	−0.96506776[8]
a_7	0.13859162 [8]	0.52001434 [9]
a_8	−0.10638816[8]	−0.86789973[9]
a_9	−0.26604647[9]	−0.44938816[8]
a_{10}	0.66039444 [9]	0.54194416 [9]
a_{11}	−0.63085775[8]	0.10897184 [10]
	For $R\le R_L$ [a]	
R_L	3.68246	3.0067
c_L	0.587688 [4]	0.452737 [4]
d_L	0.854960 [7]	0.5722619 [6]
α_L	4	4
	For $R\ge R_R$ [a]	
R_R	9.80	6.3936
c_R		0.116328 [5]
d_R		−0.1171404[9]
α_R		4.42294

Spin-orbit parameters[b]

	Δ_{od}	Δ_d
$p(1)$(Fixed)	112.005	79.200
$p(2)$	75.057(70)	61.611(800)
$p(3)$	5.4940	6.1465
$p(4)$	0.40168	0.41377

[a]Equation (7).
[b]Equation (8).

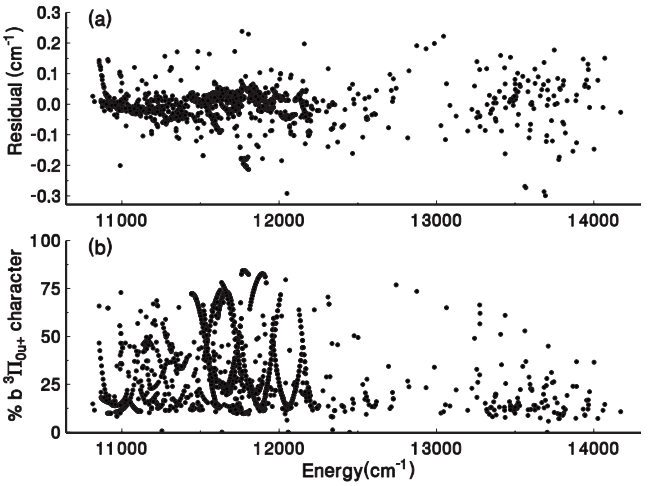

FIG. 4. (a) Residuals of the $A\ ^1\Sigma_u^+$-$b\ ^3\Pi_{0u+}$ fit. The rms residual was 0.053 cm^{-1}. (b) The percentage of the triplet component in the highly perturbed levels A-b complex. Almost 20% of the observed levels have a percentage of triplet character higher than 50% and most of these occur below 12 000 cm^{-1}.

isotopic mass, nonetheless, the data on the $^{85}Rb^{87}Rb$ and $^{87}Rb_2$ isotopomers were important for the determination of the vibrational numbering of the $b\ ^3\Pi_{0u+}$ manifold.

To indicate the quality of the fit, the residuals for each term value are plotted in Fig. 4(a). Almost 80% of the observed levels have a dominant singlet character and the rest have triplet character as shown in Fig. 4(b).

The fitted potentials, along with *ab initio* adiabatic potentials from [64] are shown in Fig. 5.

Calculated and observed term values showing the extent of the perturbed data for low vibrational levels of the A state are presented in Fig. 6. In this plot, $0.017J(J+1)$ has been subtracted from each term value so as to clarify the extent of data in each vibrational level and to display the perturbation effects more clearly. As can be seen, some of the observed rotational sequences in low levels of the A state penetrate the avoided crossing zones and thereby provide accurate information on the spin-orbit coupling functions. More extensive plots of term values, covering the full range of the data used in this work, are given in [49].

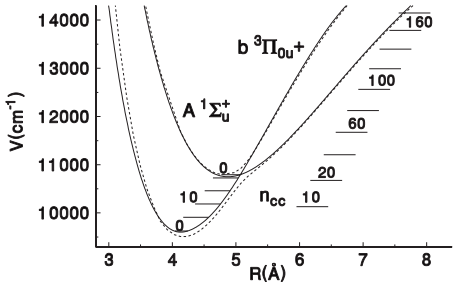

FIG. 5. Fitted diabatic potentials for $A\ ^1\Sigma_u^+$ and $b\ ^3\Pi_{0u+}$ states (solid curves) in comparison with *ab initio* adiabatic potentials from [64] (dashed lines). Above $v=2$ of the A state, vibrational levels are too highly mixed to assign to one state or the other. The coupled-channels eigenstates are labeled by n_{cc} (not a quantum number), which simply counts levels of both A and b states.

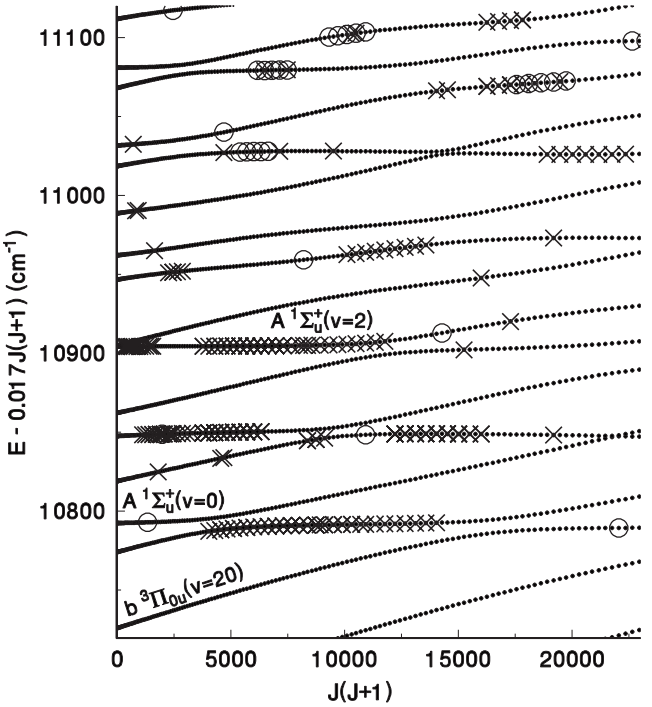

FIG. 6. For $^{85}Rb_2$, observed energies and energies calculated from a two-channel Hamiltonian shown for the region near $v=0$ of the $A\ ^1\Sigma_u^+$ state and above. $0.017J(J+1)$cm^{-1} has been subtracted from the energies so as to approximately remove the rotational energy and keep an entire vibronic level within the plotted area. Dots represent calculated term values for the A and b states. Crosses and circles represent experimental data obtained at Lyon and Orsay, respectively. The mixing between singlet and triplet characters becomes very strong above $v=2$ of the A state.

Figure 6 also shows that in the region of the low vibrational levels of the A state, levels that are predominantly $b\ ^3\Pi_{0u+}$ are distinguished from those that are predominantly $A\ ^1\Sigma_u^+$ by having steeper slopes of energy vs $J(J+1)$. At higher energies, beginning actually with $A(v=3)$, the behavior of energy vs $J(J+1)$ often exhibits an intermediate slope, indicating that these wave functions have a highly mixed character.

Another perspective on the mixing of the two wave-function components is shown in Fig. 7, which displays results for $J=0$ wave functions from two-channel calculations. For the level at 10 791.4 cm^{-1} (top plot), the A component is significantly larger than the $b\ ^3\Pi_{0u+}$ component. However, the singlet-triplet mixing is larger than might be expected from considering Fig. 6 because in this region, the wave functions are associated with the adiabatic potentials shown as dashed lines in Fig. 5 (from *ab initio* calculations), which change character with R. For the other two cases, the overall fraction of A character is smaller, but in certain small regions of R, the A character dominates. This behavior will be reflected in calculated Franck-Condon factors, which depend on the overlap of particular components with other particular wave functions.

Figure 7 also displays the special properties of coupled-channel wave functions. The solid lines in the bottom two plots, in particular, show that the nominally $A\ ^1\Sigma_u^+$ channel

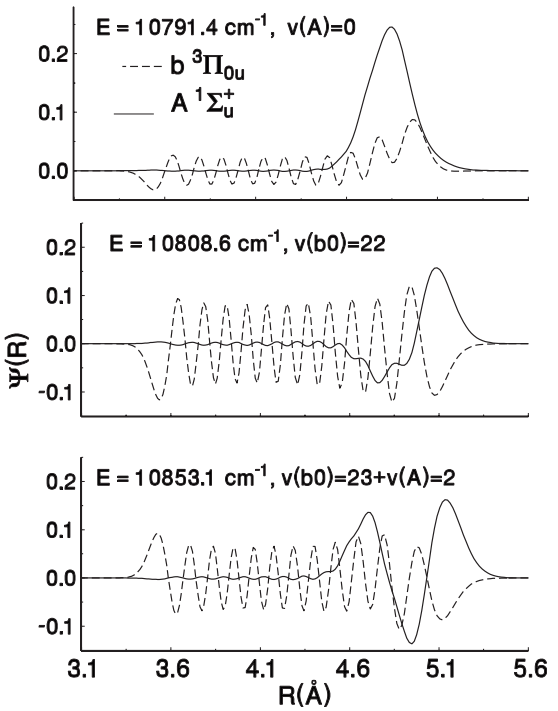

FIG. 7. Two-channel wave functions for $J=0$, showing the relative contributions of the singlet and triplet components for three eigenfunctions at energies near $A(v=0)$. Note that the component wave functions are *not* eigenfunctions of the separate singlet and triplet potentials.

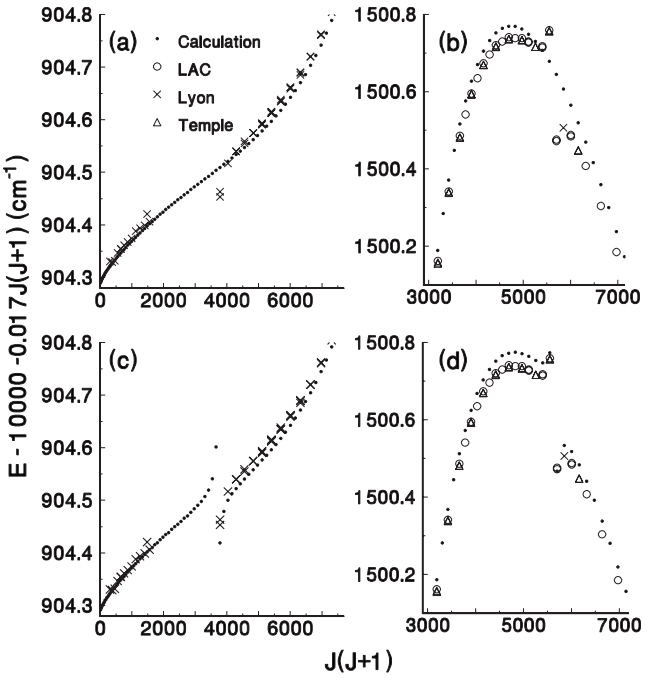

FIG. 8. Observed and calculated term values in regions where avoided crossings occur in the rotational progressions, due to the presence of $b\ ^3\Pi_1$ levels. (a) and (b) show calculated two-channel eigenvalues, while (c) and (d) show four-channel eigenvalues in which the $\Omega=1$ levels appear.

wave function acquires some of the shorter-wavelength oscillations of the $b\ ^3\Pi_{0u+}$ channel. In the DVR Hamiltonian, at each value of R, there exists both (1) coupling elements along the diagonal of the off-diagonal blocks and (2) mixing with other R values in the same channel by the kinetic-energy operator. Since (1) and (2) act simultaneously, each component of each coupled-channel eigenfunction contains some effects of mixing between singlet and triplet.

After fits with the two-channel Hamiltonian had converged, we noticed several regions in which avoided crossings in the rotational progressions could be identified that were not associated with coupling between $A\ ^1\Sigma_u^+$ and $b\ ^3\Pi_{0u+}$ levels as depicted in Fig. 6. We attributed these additional avoided crossings to the effect of $b\ ^3\Pi_{1u}$ levels, which are coupled to the $\Omega=0$ component of the mixed states by the $\langle {}^3\Pi_0|H|{}^3\Pi_1\rangle$ element in Eq. (4). Accordingly, we introduced fine-structure splitting and this Coriolis term into three-channel and four-channel Hamiltonian matrices. By trial and error adjustments of the p_i parameters for Δ_d, we were able to model quite accurately all six regions of avoided crossings in the rotational structure, ranging from $E=10\ 967$ to 11806 cm^{-1}. Two such cases are shown in Fig. 8, which shows results from both two-channel and three-channel calculations.

When the fine-structure splitting was modeled as discussed above, the rms residual diminished from 0.067 cm^{-1} to the value of 0.053 cm^{-1} quoted above. To obtain an estimate for the $\Delta_d(R)$ function, the lengthy progressions of rotational lines were crucial. Note also that Fig. 8, with its magnified energy scale, shows the quality of the fits more clearly than Fig. 6, which more generally shows the extent of the data over the plotted region. The Morse-function parameters p_i for Δ_d are given in Table I.

Despite the addition of $b\ ^3\Pi_{1u}$ and $b\ ^3\Pi_{2u}$ components to the Hamiltonian, there were certain regions where systematic deviations between observed and fitted term values persisted. Figure 9 shows a region in which the rotational progression exhibits an anomalously narrow $^1\Sigma_u^+$-$^3\Pi_{0u+}$ avoided crossing, evidently due to an effective cancellation in the coupling element. It is possible that these levels are especially sensitive to higher-order effects or these residuals may be demonstrating that the Morse-function form of the off-diagonal spin-orbit function is inadequate. However, in contrast to the situation with the A and b states of Na_2 [16], the use of the

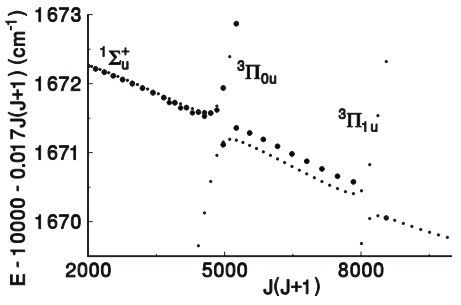

FIG. 9. Observed and calculated term values near an anomalously narrow $A\ ^1\Sigma_u^+$-$b\ ^3\Pi_{0u+}$ avoided crossing, showing relatively large residuals that repeated efforts in the fitting procedure failed to significantly diminish. Large dots represent experimental term values; small dots are term values calculated with fitted parameters.

TABLE II. Comparison of present results with *ab initio* potential parameters. T_e and ω_e are in cm^{-1}, R_e is in Å. To obtain values for $b\ ^3\Pi_{1u}$ from the present work (PW), $\Delta_d(R)$ was added to the fitted potential for $b\ ^3\Pi_{0u+}$.

	$A\ ^1\Sigma_u^+$ state			$b\ ^3\Pi_{1u}$ state		
Ref.	T_e	R_e	ω_e	T_e	R_e	ω_e
[65] 1989	10946	4.73	49	10163	4.05	57
[66] 1990	10910	4.83	44.7	8470	4.51	42.9
[67] 1992	10723	4.85	44			
[63] 2001	10829	4.90	44	9779	4.20	59
[68] 2003	11073	4.88	44.2	10145	4.19	55.0
[64] 2006				9631	4.17	55.4
[69] 2006	10853	4.87	44.2	9996	4.16	50.9
PW(ECP-CPP-CI)	10915	4.90	43.8	9777	4.19	57.7
PW(expt)	10749.74	4.87	44.6	9691	4.13	59.3

ab initio spin-orbit functions rather than fitted SO functions in the least-squares fit did not diminish the variance.

The potential parameters a_k and the fitted values of T_e and R_e for the $A\ ^1\Sigma_u^+$ and $b\ ^3\Pi_u$ states from a four-channel Hamiltonian calculation are listed in Table I.

The vibrational parameters ω_e given in Table I have been obtained from Eq. (6) using the fitted values for a_2, R_e, and b. Table II presents a comparison of the present results with parameters from *ab initio* calculations.

IV. SPIN-ORBIT FUNCTIONS

The spin-orbit coupling manifests itself in the excited spectrum of all alkali-metal molecules and is especially important in the heavier species such as Rb_2. In the atomic limit, the splitting of the excited ^2P energy level into sublevels $^2P_{1/2}$ and $^2P_{3/2}$ gives rise to two lines in the atomic spectra of alkali metals. These spin-orbit effects are due to the interaction of the spinning electron with the magnetic field created by its orbital motion around the nucleus. In this work, empirical spin-orbit functions are obtained by fitting the term value data. We also present *ab initio* spin-orbit functions from two different approaches. Numerical data for both the empirical and *ab initio* spin-orbit functions are given in [49].

A. Fitted spin-orbit functions

The fitted spin-orbit functions deduced from four-channel computation are given in Table I. Figure 10 shows the fitted diagonal and off-diagonal spin-orbit functions, together with *ab initio* functions discussed below. However, it is important to recognize the limitations of the fit results for these functions.

For smaller SO off-diagonal coupling functions, such as what occur in the light alkali-metal dimers, the principle of stationary phase [70] states that only the value of the coupling function at the potential crossing point R_c is sampled by experimental observations. As indicated in Fig. 10, for the Rb_2 $A\ ^1\Sigma_u^+$ and $b\ ^3\Pi_{0u^+}$ potentials, R_c=5.07 Å. For the analogous states in Na_2 [16], a wide variety of coupling functions having identical values at $R=R_c$ gave comparably good fits to the data. For the large SO coupling function here, the restriction imposed by the stationary phase approximation is relaxed, and the quality of the fit does indeed depend on the shape of the function as well as its value at R_c. Although they could not be fit explicitly, optimum values of $p(3)$ and $p(4)$ were obtained by fixing these parameters over a range of values and fitting 10 to 26 other parameters to the data. Furthermore, when an exponential damping function $f_D=1-\alpha\exp(-\beta R)$ was placed in front of the $\Delta_{od}(R)$ Morse-type function, the fit results overcompensated by favoring an even steeper rise at small R, giving further support to the conclusion that the data prefer that Δ_{od} rises as R decreases beyond a certain value. However, it is undoubtedly the case that values of $\Delta_{od}(R)$ near R_c are most important in the fitting process.

For the diagonal spin-orbit function $\Delta_d(R)$, observations in different vibrational levels sample different values of $\langle R\rangle$. Here, $\langle R\rangle$ values shown in Fig. 10 have been obtained from the expectation value over R of the $^3\Pi_{1u}$ component of the coupled-channels wave function, corresponding to observed levels that exhibit the maximum $^3\Pi_{1u}$ character. For Na_2 [16], $\Delta_d(R)$ was convincingly shown to be a decreasing function of R over a significant range of $\langle R\rangle$ values. In the present work, the observed cases of fine-structure splitting provide a much smaller range of $\langle R\rangle$ values than was the case in [16]; but, nevertheless, $\Delta_d(R)$ clearly exhibits a negative slope over this region.

The derived $\Delta_d(R)$ function is based on the differences between observed mostly $^3\Pi_{1u}$ levels and the deperturbed $^3\Pi_{0u+}$ energies obtained from the fit. Therefore, $\Delta_d(R)$ includes second-order effects due to coupling between $b\ ^3\Pi_{1u}$ and other $\Omega=1u$ states associated with the $5\ ^2S+5\ ^2P$ limit, namely, the $B\ ^1\Pi_u$ and (2) $^3\Sigma_u^+$ states. An empirical B state potential function can be constructed from information in [71], and an *ab initio* (2) $^3\Sigma_u^+$ potential has been calculated by [64] and others. Using *ab initio* spin-orbit functions calculated by the ECP-CPP-CI approach defined below, we find that the second-order spin-orbit perturbation shift from the B

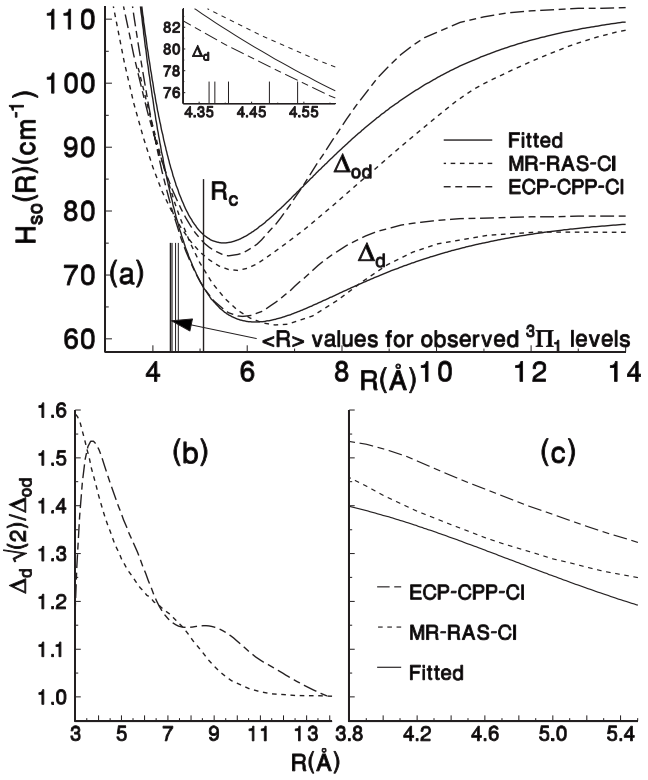

FIG. 10. (a) Fitted and *ab initio* diagonal and off-diagonal spin-orbit functions. $\langle R\rangle$ values for the limited number of observed $b\ ^3\Pi_{1u}$ levels are denoted by thin vertical lines; while R_c, the R value at the $A\ ^1\Sigma_u^+$-$b\ ^3\Pi_{0u^+}$ crossing, is identified by a longer vertical line. The *ab initio* results are obtained by authors (S.K.) (MR-RAS-CI) and (A.V.S.) (ECP-CPP-CI). The inset shows values of $\Delta_d(R)$ for R values over the region of the observed $\langle R\rangle$. (b) For the two *ab initio* methods, this plot shows the ratio Δ_d to $\Delta_{od}/\sqrt{(2)}$, which is unity in the large R limit. (c) The same ratio as in (b) from the *ab initio* functions and also the fitted function over the R range for which the fitted function is most accurate.

state dominates and varies from 1.6 to 1.3 cm^{-1} over the range of $\langle R\rangle$ values of 4.3 to 4.6 Å. Hence, the deperturbed $\Delta_d(R)$ functions would be larger than that shown in Fig. 10 by these amounts.

In the large R limit, Δ_{od} is larger than Δ_d by $\sqrt{(2)}$. It is interesting to ask what is this ratio for finite R and how the ratio from the fitted spin-orbit functions agree with that for the *ab initio* functions. Figure 10(b) shows the ratio for the two *ab initio* functions out to large R and Fig. 10(c) shows also the ratio for the fitted functions over the R range in which they are most accurate. The ratio for the effective core pseudopotential core-polarization potential-configuration interaction (ECP-CPP-CI) approach agrees within about 3% with the ratio from the empirical functions and, thus, the difference is just somewhat larger than the uncertainty in the experimental values.

B. *Ab initio* spin-orbit functions

Corroboration of the spin-orbit functions from *ab initio* calculations is of considerable interest for Rb_2. These calculations are much more difficult than for lighter alkali-metal atoms. An extensive study of the spin-orbit coupling has been conducted over the years on molecules lighter than Rb_2 (see, for example, [12,60,72–76]). The only paper, to our knowledge, that gives a detailed account of the R-dependent spin-orbit effects in Rb_2 is Ref. [68]. In this paper, authors describe all-electron relativistic calculations of the Rb_2 ground and excited potentials as well as the diagonal and off-diagonal spin-orbit matrix elements between the low-excited electronic potentials using the quasidegenerate perturbation theory. As was pointed out in [68], this perturbative approach underestimates the spin-orbit splitting at the asymptotic limit of the ^2P term by 30%.

Here we apply two different computational quantum-chemistry methods to obtain spin-orbit coupling matrix elements. The first method, the multireference restricted-active-space CI (MR-RAS-CI) method (work at Temple University), includes all electrons of the Rb_2 molecule and uses nonrelativistic numerical Hartree-Fock and Sturm functions or molecular orbitals (MOs) as a basis set. The second method (work at Moscow State University) based on a full valence CI procedure uses the ECP, the CPP, and a Gaussian basis set for valence electrons. More details on both methods are given below. A comparison of the results of these two methods and the fitted spin-orbit matrix elements allows us to feel confident about our predictions.

The MR-RAS-CI method partitions occupied molecular orbitals into two subsets. The subsets are the core orbitals, which do not participate in the CI procedure and active-valence orbitals from which we allow single, double, and triple excitations. In addition, we use virtual or unoccupied orbitals, which are allowed to contain up to two electrons in the CI expansion. The core and valence orbitals are Hartree-Fock functions and virtual orbitals are Sturm functions. The valence and virtual orbitals form the active orbital space. The dimensionality of the CI molecular wave function increases rapidly with the size of the active orbital space and, therefore, we applied a final restrictive measure. We divide the active orbitals into further subgroups and limit the number of excitations from each group. We believe that the above restrictions do not lead to substantial degradation of the molecular wave function.

The total molecular wave function $|\Psi\rangle$ of the nonrelativistic many-electron Hamiltonian is formed as the linear combination,

$$|\Psi\rangle = \sum_\alpha C_\alpha |\Phi_\alpha\rangle, \tag{9}$$

where $|\Phi_\alpha\rangle$ is a many-electron molecular Slater determinant, constructed as an antisymmetrized product of molecular orbitals. The CI coefficients C_α are obtained by solving a generalized eigenvalue matrix problem.

For the Rb_2 molecule, electrons up to the $3d^{10}$ shell are included in the core. The nine $4s^2$, $4p^6$, and $5s$ or $5p$ valence electrons for each atom are held in active-valence space. In addition, we use the ten virtual orbitals from $4d$ to $7d$ to complete the active space. The dynamics of all electrons in a molecule is accounted for in our calculation. This allows us to properly describe the spin-orbit effects at small internuclear separations.

The spin-orbit functions between two total molecular wave functions are the matrix elements $\langle\Psi'|H_{SO}|\Psi\rangle$, where H_{SO} is the Breit-Pauli Hamiltonian given by

$$H_{SO} = H_{sso} + H_{soo}. \tag{10}$$

The first term is a one-electron operator that describes the "spin-same-orbit" interaction, which in atomic units is given by

$$H_{sso} = \frac{\alpha^2}{2}\sum_N \sum_i \frac{Z_N}{r_{iN}^3}\vec{l}_{iN}\cdot\vec{s}_i, \tag{11}$$

where the sum N is over all nuclei and the sum i over all electrons, Z_N is the charge of nucleus N, r_{iN} denotes the distance between the ith electron and the Nth nucleus, and α is the fine-structure constant. The operator $\vec{l}_{iN}$ is the orbital angular momentum between electron i and nucleus N and $\vec{s}_i$ is the spin of electron i. The second term of Eq. (10) describes the "spin-other-orbit" contribution,

$$H_{soo} = -\frac{\alpha^2}{2}\sum_{i\neq j}\frac{1}{r_{ij}^3}[\vec{r}_{ij}\times\vec{p}_i]\cdot(\vec{s}_i + 2\vec{s}_j), \tag{12}$$

where the sums i and j are over all electrons, r_{ij} denotes the interelectron separation, and $\vec{p}_i$ is electron momentum operator.

In the ECP-CPP-CI calculations, the inner-core shells of the rubidium atom $[\mathrm{Ar}]3d^{10}$ are replaced by a spin-orbit averaged nonempirical ECP, leaving 18 outer-core and valence electrons of Rb_2 dimer for explicit treatment. The shape consistent spin-averaged and spin-orbit Gaussian basis sets come from Ref. [77], while the $[7s7p5d3f]$ Gaussian valence basis set was taken from Refs. [29,78].

The optimized MOs are constructed from the solutions of the state-averaged complete active space self-consistent field problem for the lowest $(1-4)\ ^{1,3}\Sigma^+$ and $(1-3)\ ^{1,3}\Pi$ electronic states taken with equal weights [79]. The resulting active space consists of 14σ and 10π MOs. The dynamical correlation effects are introduced by the internally contracted multireference configuration-interaction (MRCI) method [80], which is applied for only two valence electrons keeping the rest frozen, i.e., in a full valence (two-electrons) CI scheme. The l-independent CPP taken in the Müller-Meyer form [81] is employed together with the above small core ECP to take into account implicitly the residual core-polarization effects [82]. The original ECP spin-orbit Gaussian coefficients [77] are scaled by a factor of 1.17 and the exponential parameter of the CPP cutoff function $\rho_c = 0.395a_0$ is adjusted in order to reproduce the experimental fine-structure splitting of the lowest-excited $\mathrm{Rb}(5\ ^2P_{1/2;3/2})$ state. The required individual spin-orbit matrix elements for a given pair of states $\xi_{ij}^{so}(R) = \langle\Psi_i^{el}|\Sigma_i\xi_i\vec{l}_i\vec{s}_i|\Psi_j^{el}\rangle|_{\vec{\mathbf{r}}}$ are evaluated in the basis of the zeroth-order (spin-averaged) MRCI wave functions $\Psi_i^{el}(\vec{\mathbf{r}};R)$ corresponding to the pure Hund's coupling case (a) scheme. All electronic calculations are performed with the MOLPRO v.2008.1 program package [83].

Results of both *ab initio* calculations of the diagonal $\Delta_d = \langle^3\Pi|H_{SO}|^3\Pi\rangle$ and the off-diagonal $\Delta_{od} = \langle^1\Sigma^+|H_{SO}|^3\Pi\rangle$ matrix elements are shown in Fig. 10. The MR-RAS-CI calculated value for $\Delta_d(R)[\Delta_{od}(R)]$ is 76.6 cm^{-1} (109.3 cm^{-1}) at 16 Å (15.0 Å), as compared with the expected values $\Delta_a/3 = 79.2\ \mathrm{cm}^{-1}$ ($\sqrt{2}\Delta_a/3 = 112.0\ \mathrm{cm}^{-1}$) for $R\to\infty$, where Δ_a is the splitting between the atomic $^2P_{1/2}$ and $^2P_{3/2}$ levels of Rb.

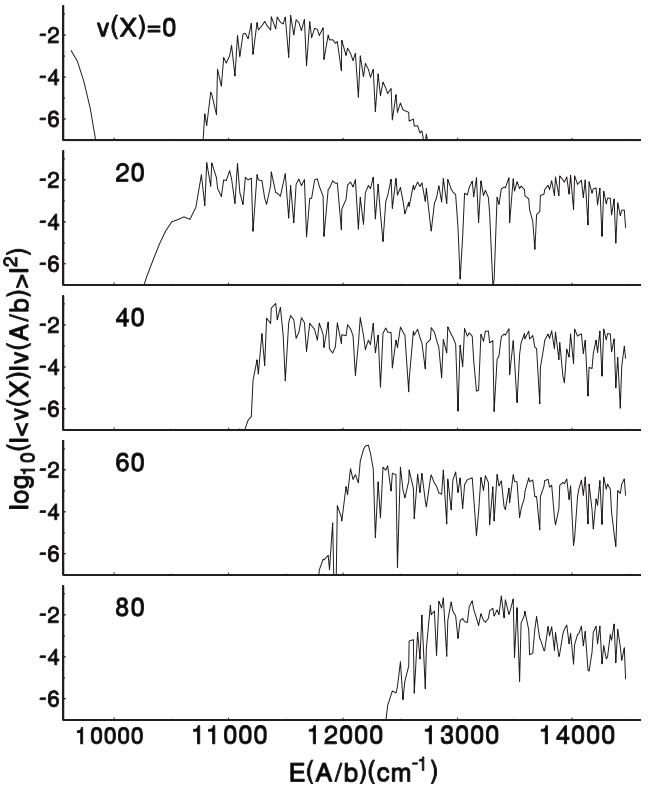

FIG. 11. Franck-Condon factors for transitions to A-b levels from various X state vibrational levels.

There are two reasons for the R dependence of the spin-orbit coupling matrix elements. First, it is due to the change in CI coefficients of the total molecular wave function with R. The second effect is the $1/r^3$ dependence of the spin-orbit Hamiltonian, where r is the distance of the electron from the nuclei, which is then reflected in an R dependence. From various test calculations, we obtain the following explanation for the form of the spin-orbit functions. The decrease in magnitude from large R to approximately 6 Å is associated with the decrease in the p atomic wave-function component in the molecular wave function over this region. The increase in magnitude of both $\Delta_d(R)$ and $\Delta_{od}(R)$ for R less then 6 Å is associated with the penetration of the $5p$ electron, which has an average radius of 4.0 Å, of one atom into the core orbitals of the other. The $5p$ electron probability density near the $5s$ atom excites some of the core electrons on this atom producing open inner-shell orbitals. In addition, the spin-same-orbit interaction of the $5p$ electron near the $5s$ atomic nucleus and the spin-other-orbit interactions in this region also enhance the spin-orbit effect as R decreases.

V. FRANCK-CONDON FACTORS

One motivation for acquiring and analyzing data on the A and b states of Rb_2 is to facilitate the production of cold

molecules using excitation from Feshbach resonance states. The scheme as demonstrated in [10] with Cs_2 could also be used with Rb_2, although the required magnetic field may be much larger. One might imagine excitation from the Feshbach resonance at 1007 G [84] to some A-b level followed by a stimulated decay to an X state level bound to some degree followed by a second excitation to another A-b level and stimulated decay to $v=0$ of the X state. However, our estimate of the 1007 G Feshbach resonance $X\ ^1\Sigma_g^+$ component wave function indicates that the predominant antinode occurs near 30 Å and, thus, would lead to adequate excitation strengths for higher levels of the $A\ ^1\Sigma_u^+$ state than are included in the present analysis. We present plots of A-$b \leftarrow X$ Franck-Condon factors over a range of vibrational levels of the X state and A-b level energies, in Fig. 11, to give an estimate of the limitations on the range of $v(X)$ that the second step imposes on the first step of transfer from the Feshbach resonance. In addition, [49] includes tables of Franck-Condon factors for (a) excitations from X state levels $v'=0-15$, $J'=0$, 40, 80, 120, and 160 and (b) for excitations from X state $J'=0$, $v'=0-122$.

VI. CONCLUSION

The detailed energy-level structure of the strongly coupled $A\ ^1\Sigma_u^+$-$b\ ^3\Pi_u$ states of Rb_2 has remained an unresolved problem for a long time due to inadequate data, and also because numerical methods for modeling such cases of strong spin-orbit coupling have been developed only recently. Additional high-resolution Fourier transform spectra (FTS) obtained by the LIF technique, together with optical-optical double-resonance polarization techniques, have significantly extended the available data. FTS data on the lowest vibrational levels ($v' \leq 3$) of the $A\ ^1\Sigma_u^+$ state to the ground state have been especially useful in characterizing both the A and the b states.

Some six instances of avoided crossings in extended rotational progressions have been identified as due to $^3\Pi_{1u}$ levels. From these cases, three- and four-channel calculations have made possible a characterization of the spin-orbit splitting in the b state. Both this "diagonal" spin-orbit splitting as well as the "off-diagonal" spin-orbit function connecting the $A\ ^1\Sigma_u^+$ and $b\ ^3\Pi_{0u+}$ states exhibit a Morse-function-like form, as found in other alkali dimer species. Analysis of the *ab initio* wave functions for Rb_2 indicate that this form is due to a decrease in p character in the wave function as R decreases from ∞, together with an overlap of p electrons from one nucleus with the s and core electrons on the other nucleus, at small values of R. The spin-other-orbit part of the Hamiltonian plays an important role in the latter regime.

An extension of this analysis to higher energies could provide a direct link between the spectroscopic and photoassociation data on 0_u^+ states of Rb_2 [20].

ACKNOWLEDGMENTS

We are grateful to C. Amiot for providing the LAC data and to M. Aubert-Frécon for communicating unpublished Rb_2 potentials. The work at Stony Brook was supported by the NSF Grant No. PHY0652459 and at Temple University by the NSF Grant No. PHY0555608 and by the ARO and AFOSR.

[1] See, for example, L. Li and A. M. Lyyra, Spectrochim. Acta, Part A **55**, 2147 (1999) on the use of window states to excite higher triplet states of Li_2 and Na_2.
[2] J. M. Sage, S. Sainis, T. Bergeman, and D. DeMille, Phys. Rev. Lett. **94**, 203001 (2005).
[3] J. Deiglmayr, A. Grochola, M. Repp, K. Mörtlbauer, C. Glück, J. Lange, O. Dulieu, R. Wester, and M. Weidemüller, Phys. Rev. Lett. **101**, 133004 (2008).
[4] S. Ospelkaus, A. Pe'er, K.-K. Ni, J. J. Zirbel, B. Neyenhuis, S. Kotochigova, P. S. Julienne, J. Ye, and D. S. Jin, Nat. Phys. **4**, 622 (2008).
[5] K.-K. Ni, S. Ospelkaus, M. H. G. de Miranda, A. Pe'er, B. Neyenhuis, J. J. Zirbel, S. Kotochigova, P. S. Julienne, D. S. Jin, and J. Ye, Science **322**, 231 (2008).
[6] F. Lang, K. Winkler, C. Strauss, R. Grimm, and J. Hecker Denschlag, Phys. Rev. Lett. **101**, 133005 (2008).
[7] C. M. Dion, C. Drag, O. Dulieu, B. Laburthe Tolra, F. Masnou-Seeuws, and P. Pillet, Phys. Rev. Lett. **86**, 2253 (2001).
[8] M. Viteau, A. Chotia, M. Allegrini, N. Bouloufa, O. Dulieu, D. Comparat, and P. Pillet, Science **321**, 232 (2008).
[9] J. Danzl, E. Haller, M. Gustavsson, M. J. Mark, R. Hart, N. Bouloufa, O. Dulieu, H. Ritsch, and H.-C. Nägerl, Science **321**, 1062 (2008).
[10] M. J. Mark, J. G. Danzl, E. Haller, M. Gustavsson, N. Bouloufa, O. Dulieu, H. Salami, T. Bergeman, H. Ritsch, R. Hart and H.-C. Nägerl, Appl. Phys. B **95**, 219 (2009).
[11] C. Lisdat, O. Dulieu, H. Knöckel, and E. Tiemann, Eur. Phys. J. D **17**, 319 (2001).
[12] M. R. Manaa, A. J. Ross, F. Martin, P. Crozet, A. M. Lyyra, L. Li, C. Amiot, and T. Bergeman, J. Chem. Phys. **117**, 11208 (2002).
[13] T. Bergeman, C. E. Fellows, R. F. Gutterres and C. Amiot, Phys. Rev. A, **67**, 050501(R) (2003).
[14] O. Docenko, M. Tamanis, R. Ferber, E. A. Pazyuk, A. Zaitsevskii, A. V. Stolyarov, A. Pashov, H. Knöckel, and E. Tiemann, Phys. Rev. A **75**, 042503 (2007).
[15] J. Zaharova, M. Tamanis, R. Ferber, A. N. Drozdova, E. A. Pazyuk, and A. V. Stolyarov, Phys. Rev. A **79**, 012508 (2009).
[16] P. Qi, J. Bai, E. Ahmed, A. M. Lyyra, S. Kotochigova, A. J. Ross, C. Effantin, P. Zalicki, J. Vigué, G. Chawla, R. W. Field, T.-J. Whang, W. C. Stwalley, H. Knöckel, E. Tiemann, J. Shang, L. Li, and T. Bergeman, J. Chem. Phys. **127**, 044301 (2007).
[17] A. Derevianko, Phys. Rev. A **67**, 033607 (2003).
[18] M. Anderson, J. R. Ensher, M. R. Matthews, C. E. Wieman, and E. A. Cornell, Science **269**, 198 (1995).
[19] J. D. Miller, R. A. Cline, and D. J. Heinzen, Phys. Rev. Lett. **71**, 2204 (1993).

[20] T. Bergeman, J. Qi, D. Wang, Y. Huang, H. K. Pechkis, E. E. Eyler, P. L. Gould, W. C. Stwalley, R. A. Cline, J. D. Miller, and D. J. Heinzen, J. Phys. B **39**, S813 (2006).
[21] K. M. Jones, E. Tiesinga, P. D. Lett, and P. S. Julienne, Rev. Mod. Phys. **78**, 483 (2006).
[22] W. C. Stwalley, Eur. Phys. J. D **31**, 221 (2004).
[23] H. Salami, T. Bergeman, J. Danzl, C.-H. Nägerl, O. Dulieu, D. Li, F. Xie, and L. Li (unpublished).
[24] A. J. Ross, C. Effantin, J. d'Incan, and R. F. Barrow, Mol. Phys. **56**, 903 (1985).
[25] A. J. Ross, C. Effantin, J. d'Incan, and R. F. Barrow, J. Phys. B **19**, 1449 (1986).
[26] A. J. Ross, R. M. Clements, and R. F. Barrow, J. Mol. Spectrosc. **127**, 546 (1988).
[27] H. Sun and J. Huennekens, J. Chem. Phys. **97**, 4714 (1992).
[28] R. Ferber, E. A. Pazyuk, A. J. Stolyarov, A. Zaitsevskii, H. Chen, H. Wang, and W. C. Stwalley, J. Chem. Phys. **112**, 5740 (2000).
[29] M. Tamanis, R. Ferber, A. Zaitsevskii, E. A. Pazyuk, A. V. Stolyarov, H. Chen, J. Qi, H. Wang, and W. C. Stwalley, J. Chem. Phys. **117**, 7980 (2002).
[30] X. Xie and R. W. Field, Chem. Phys. **99**, 337 (1985).
[31] X. Xie and R. W. Field, J. Mol. Spectrosc. **117**, 228 (1986).
[32] C. Linton, F. Martin, I. Russier, A. J. Ross, P. Crozet, S. Churassy, and R. Bacis, J. Mol. Spectrosc. **175**, 340 (1996).
[33] K. Urbanski, S. Antonova, A. M. Lyyra, A. Yiannopoulou, and W. C. Stwalley, J. Chem. Phys. **104**, 2813 (1996).
[34] J. B. Atkinson, J. Becker, and W. Demtröder, Chem. Phys. Lett. **87**, 92 (1982).
[35] C. Effantin, O. Babaky, K. Hussein, J. d'Incan, and R. F. Barrow, J. Phys. B **18**, 4077 (1985).
[36] T.-J. Whang, W. C. Stwalley, L. Li, and A. M. Lyyra, J. Chem. Phys. **97**, 7211 (1992).
[37] H. Katô, M. Otani, and M. Baba, J. Chem. Phys. **89**, 653 (1988).
[38] A. J. Ross, P. Crozet, C. Effantin, J. d'Incan, and R. F. Barrow, J. Phys. B **20**, 6225 (1987).
[39] A. M. Lyyra, W. T. Luh, L. Li, H. Wang, and W. C. Stwalley, J. Chem. Phys. **92**, 43 (1990).
[40] G. Jong, L. Li, T.-J. Whang, A. M. Lyyra, W. C. Stwalley, M. Li, and J. Coxon, J. Mol. Spectrosc. **155**, 115 (1992).
[41] J. T. Kim, H. Wang, C. C. Tsai, J. T. Bahns, W. C. Stwalley, G. Jong, and A. M. Lyyra, J. Chem. Phys. **102**, 6646 (1995).
[42] C. Amiot, O. Dulieu, and J. Vergès, Phys. Rev. Lett. **83**, 2316 (1999).
[43] J. Y. Seto, R. Le Roy, J. Vergès, and C. Amiot, J. Chem. Phys. **113**, 3067 (2000).
[44] The Aimé Cotton Iodine Atlas, S. Gerstenkorn and P. Luc, Atlas du Spectre d'Absorption de la Molecule d'Iode, Editions du CNRS, Paris, 1978, was recalibrated in 1979 by S. Gerstenkorn and P. Luc, Rev. Phys. Appl. **14**, 791 (1979).
[45] H. Salami and A. J. Ross, J. Mol. Spectrosc. **233**, 157 (2005).
[46] C. Amiot and J. Vergès, Chem. Phys. Lett. **274**, 91 (1997).
[47] B. A. Palmer, R. A. Keller, and R. Engleman, Jr., LASL Report No. LA-8251-MS (Los Alamos Scientific Laboratory, Los Alamos, NM, 1980).
[48] G. O. Sitz and R. L. Farrow, J. Chem. Phys. **101**, 4682 (1994).
[49] See EPAPS Document No. E-PLRAAN-80-002908 for files that give fitted parameters and potential curves, fitted and *ab initio* spin-orbit functions, Franck-Condon factors, and lists and also plots of observed and fitted term values. For more information on EPAPS, see http://www.aip.org/pubservs/epaps.html.
[50] R. Meyer, J. Chem. Phys. **52**, 2053 (1970).
[51] R. Kosloff, J. Phys. Chem. **92**, 2087 (1988).
[52] D. Colbert and W. H. Miller, J. Chem. Phys. **96**, 1982 (1992).
[53] O. Dulieu and P. S. Julienne, J. Chem. Phys. **103**, 60 (1995).
[54] E. Tiesinga, C. J. Williams, and P. S. Julienne, Phys. Rev. A **57**, 4257 (1998).
[55] V. V. Meshkov, A. V. Stolyarov, and R. J. Le Roy, Phys. Rev. A **78**, 052510 (2008).
[56] R. W. Field and H. Lefebvre-Brion, *The Spectra and Dynamics of Diatomic Molecules* (Elsevier, Amsterdam, 2004).
[57] T. Bergeman, P. S. Julienne, C. J. Williams, E. Tiesinga, M. R. Manaa, H. Wang, P. L. Gould, and W. C. Stwalley, J. Chem. Phys. **117**, 7491 (2002).
[58] C. Samuelis, E. Tiesinga, T. Laue, M. Elbs, H. Knöckel, and E. Tiemann, Phys. Rev. A **63**, 012710 (2000).
[59] R. J. Le Roy, Can. J. Phys. **52**, 246 (1974).
[60] M. R. Manaa, Int. J. Quantum Chem. **75**, 693 (1999).
[61] A. V. Stolyarov (private communication).
[62] D. A. Steck, Rubidium 85 D Line Data (2002) (http://steck.us.alkalidata) revision 0.5.
[63] S. J. Park, S. W. Suh, Y. S. Lee, and G.-H. Jeung, J. Mol. Spectrosc. **207**, 129 (2001).
[64] M. Aubert-Frécon (private communication).
[65] F. Spiegelmann, D. Pavolini, and J.-P. Daudey, J. Phys. B **22**, 2465 (1989).
[66] M. Krauss and W. J. Stevens, J. Chem. Phys. **93**, 4236 (1990).
[67] M. Foucrault, P. Millié, and J.-P. Daudey, J. Chem. Phys. **96**, 1257 (1992).
[68] D. Edvardsson, S. Lunell, and C. M. Marian, Mol. Phys. **101**, 2381 (2003).
[69] J. Lozeille, A. Fioretti, C. Gabbanini, Y. Huang, H. K. Pechkis, D. Wang, P. L. Gould, E. E. Eyler, W. C. Stwalley, M. Aymar, and O. Dulieu, Eur. Phys. J. D **39**, 261 (2006).
[70] J. Tellinghuisen, J. Mol. Spectrosc. **103**, 455 (1984).
[71] C. Amiot, J. Chem. Phys. **93**, 8591 (1990).
[72] R. K. Hinkley, T. E. H. Walker, and W. G. Richards, Mol. Phys. **24**, 1095 (1972).
[73] P. W. Abegg, Mol. Phys. **30**, 579 (1975).
[74] W. G. Richards, H. T. Triveli, and D. L. Cooper, *Spin-Orbit Coupling in Molecules* (Clarendon Press, Oxford, 1981), p. 105.
[75] S. R. Langhoff, M. L. Sink, R. H. Pritchard, and W. Kern, J. Mol. Spectrosc. **96**, 200 (1982).
[76] B. F. Minaev and L. B. Yashchuk, Opt. Spectrosc. **95**, 553 (2003).
[77] L. A. LaJohn, P. A. Christiansen, R. B. Ross, T. Atashroo, and W. C. Ermler, J. Chem. Phys. **87**, 2812 (1987).
[78] A. J. Sadlej and M. Urban, J. Mol. Struct.: THEOCHEM **234**, 147 (1991).
[79] H.-J. Werner and P. J. Knowles, J. Chem. Phys. **82**, 5053 (1985).
[80] P. J. Knowles and H.-J. Werner, Theor. Chim. Acta **84**, 95 (1992).
[81] W. Müller, J. Flesch, and W. Meyer, J. Chem. Phys. **80**, 3297 (1984).
[82] I. S. Lim, W. C. Lee, Y. S. Lee, and G.-H. Jeung, J. Chem. Phys. **124**, 234307 (2006).

[83] H.-J. Werner, P. J. Knowles, R. Lindh, F. R. Manby, M. Schutz, P. Celani, T. Korona, G. Rauhut, R. D. Amos, A. Bernhardsson, A. Berning, D. L. Cooper, M. J. O. Deegan, A. J. Dobbyn, F. Eckert, C. Hampel, G. Hetzer, A. W. Lloyd, S. J. McNicholas, W. Meyer, M. E. Mura, A. Nicklass, P. Palmieri, U. Schumann, H. Stoll, A. J. Stone, R. Tarroni, and T. Thosteinsson, MOLPRO, version 2008.1, a package of *ab initio* programs.

[84] A. Marte, T. Volz, J. Schuster, S. Dürr, G. Rempe, E. G. M. van Kempen, and B. J. Verhaar, Phys. Rev. Lett. **89**, 283202 (2002).